Green Chemistry

PAPER

View Article Online
View Journal | View Issue

Cite this: *Green Chem.*, 2022, **24**, 4119

Sustainable lithium-ion batteries based on metal-free tannery waste biochar†

Pejman Salimi, [a,b] Sebastiano Tieuli, [c] Somayeh Taghavi, [c] Eleonora Venezia,[a,b] Silvio Fugattini, [a] Simone Lauciello,[a] Mirko Prato, [a] Sergio Marras,[a] Tao Li,[d] Michela Signoretto, [c] Paola Costamagna [b] and Remo Proietti Zaccaria *[a,e]

Received 21st December 2021,
Accepted 7th April 2022

DOI: 10.1039/d1gc04772h

rsc.li/greenchem

In the present study, we tackle the sustainable batteries topic by addressing its most defining aspects, namely what kind of waste material should be employed and its treatment for realizing performant battery anodes. In this regard, we focus on leather shaving waste (LSW), as it is an important waste element in many economies, resulting in an advantageous choice both from an environmental point of view and in terms of the circular economy. Herein, especially metal-free LSW is used to introduce an innovative kind of eco-friendly anode for lithium-ion batteries (LIBs). A pyrolysis process of the waste material is adopted to form biochar, followed by its texture engineering through either steam or CO_2, both of them recognized as safe and environmentally friendly procedures. Indeed, these procedures develop hierarchical micro/mesopores in the biochar and modify the amount of oxygen-containing functional groups on its surface, which can lead to high-performance anodes. In this respect, when a water-based solvent and carboxymethyl cellulose (CMC) binder are employed, the fabricated electrode discloses high initial capacities and remarkable electrochemical stability in lithium-metal half-cells. In particular, the steam-activated electrode demonstrates a specific discharge capacity of 735 mA h g^{-1} after 1000 charge and discharge cycles at 0.5 A g^{-1}. This anode electrode also secures an excellent initial capacity and acceptable cycling stability in full-cell LIBs where a high mass $LiFePO_4$ loading cathode is employed. The results reported here represent a noticeable improvement with respect to the state of the art, hence demonstrating the enormous potential associated with the green re-use of waste materials in important sectors such as energy storage.

1. Introduction

The ever-growing demand for electricity supply has been leading to a strong push towards sustainable and alternative energy sources, such as wind and solar-based generators.[1] This activity has contributed to an enhanced interest in energy accumulators, thus driving the research to design and develop high-performance energy storage devices.[2–4] In this regard, lithium-ion batteries (LIBs) are considered the most popular energy storage system for portable electronic devices and transportation applications.[5,6] Among different types of electrochemical energy storage devices, LIBs have shown superior electrochemical performance associated with high energy density, long-term stability, good rate capability, and no memory effects.[7,8] However, LIBs still face several challenges, particularly in electrode capacity, stability, and cost, which play a crucial role in battery research.[9] Although conventional electrodes such as graphite, which is used as an anode in commercial LIBs, possess several advantages, including low cost, high conductivity, and high cyclic and thermal stability, they cannot meet the future needs of the battery industry.[10] The limited theoretical gravimetric capacity of 372 mA h g^{-1}, the poor diffusion kinetics of lithium, and the formation of lithium dendrites at low temperature and/or high current rates are the main disadvantages of graphite electrodes for application in LIBs.[11] Furthermore, graphite relies heavily on fossil

[a]*Istituto Italiano di Tecnologia, via Morego 30, Genova 16163, Italy. E-mail: Remo.Proietti@iit.it*
[b]*Department of Chemistry and Industrial Chemistry, University of Genova, via Dodecaneso 31, I-16146 Genova, Italy*
[c]*CATMAT Lab, Department of Molecular Sciences and Nanosystems, Ca' Foscari University Venice and INSTM Consortium, RU of Venice, Via Torino 155, 30172 Venezia Mestre, Italy*
[d]*Key Laboratory of Liquid-Solid Structural Evolution and Processing of Materials of Ministry of Education, State Key Laboratory of Crystal Materials, Shandong University, Jinan, 250061, PR China*
[e]*Ningbo Institute of Materials Technology and Engineering, Chinese Academy of Sciences, Ningbo 315201, China*
† Electronic supplementary information (ESI) available. See DOI: https://doi.org/10.1039/d1gc04772h

fuel-based precursors determining energy-intensive synthesis.[11–13] As alternative approaches, electrodes based on Sn, Si, Ge, Fe, or Co have been considered. Even though very attractive for their capability of storing lithium at much higher quantities than graphite, they possess few drawbacks such as poor cycling stability, large volume changes during electrochemical processes, and in some cases environmental concerns,[14–16] which limit their wide application in energy storage systems. In this respect, biochars (carbon-based materials obtained from biomass or industrial waste pyrolysis), with their reduced environmental impact and economic concerns,[17] are a natural resource representing an alternative to the aforementioned electrodes. Biochars are categorized as non-graphitic/non-graphitizable, and their performance as LIB electrodes is highly dependent on their pore structure.[18] Several methods have been developed for biochar activation (*i.e.*, pore formation combined with the change in the number of functional groups containing heteroatoms on the biochar surface) and for the design of hierarchical porous structures. Examples are given by physical or chemical activations and through the employment of templates.[19–22] The structure forming biochars is typically a disordered configuration of cross-linked carbon sheets.[23] Through high temperature processes, the cross-links can be broken forming free layers of carbon, an ideal situation for the introduction of heteroatoms such as O, N, and S. This heteroatom insertion occurs especially at the outer region of the carbon sheet configuration, while the internal region undergoes an ordering process known as localized crystallization.[24] This new ordered structure is finally responsible for augmented porosity, a crucial factor in the energy storage field. In addition, physical activation using steam, CO_2, or air can increase the volume size of biochar pores, therefore triggering the formation of micro–meso–macro hierarchical porous structures.[25]

In our previous works, we found that biochar derived from *Cladophora glomerata* green algae has a higher electrochemical capacity compared to graphite in LIBs and supercapacitors.[26,27] The main reason behind this difference is the carbon-rich structure of the synthesized biochar, with highly ordered micro/macropores, high surface area, and the presence of functional groups due to physical and chemical treatments.[28]

In the present study, activated biochar is obtained from the pyrolysis of metal-free leather shaving waste (LSW) (by GOAST technology, Green Organic Agents for Sustainable Tanneries), and it is investigated as an anode material for LIBs. The choice of LSW is related to the important role that the leather industry plays in our society from a socio-economic point of view. Indeed, there are approximately 10 000 tanneries in the world producing leather for more than 6.5 million tons per year.[29] Even though the leather industry uses a by-product from the meat industry as the raw material, it is considered an activity demanding integrated prevention and pollution control.[30] Along the entire process, from raw skins/hides to finished leather, a huge amount of solid and water waste is generated.[31] The solid wastes include materials such as fleshings, raw trimmings, shavings, and buffing dust. Leather shaving is a mechanical process that aims at reducing the tanned skin to a specific thickness before tanning and finishing.[32] This product consists mainly of collagen and a tanning agent. At present, over 85% of the world's leather processing is chrome-tanned based.[33] Consequently, large amounts of chromium-containing shaving wastes need to be treated. The major concern about the management of this kind of solid waste is ascribed to chrome content, which makes the conventional disposal methods, such as landfilling and incineration, not practicable.[34] Therefore, many efforts have been developed in recent decades for promoting eco-friendly/alternative leather production methods and more effective waste management strategies.

The potential use of leather waste in lithium metal batteries was first studied by Ashokkumar *et al.*,[35] where the authors introduced a collagen-based electrode displaying a reversible capacity of 327 mA h g^{-1} after 40 charge and discharge cycles at a low current density of 0.05 A g^{-1}. Biochar derived from leather waste was also demonstrated to be a highly efficient catalyst for oxygen reduction reaction and capable of providing high specific capacitance in a three electrode-based supercapacitor.[36,37] Despite great progress, efforts addressing the engineering of biowaste structures are still essential for achieving devices suitable for practical applications. Indeed, it is recognized that the identification of a successful strategy for the use of biowaste in the energy storage field would open a new paradigm for massive green-battery production, hence making the proposed scheme suitable for realistic scenarios. Even more, it is worth noting that through pyrolysis treatment, LSW can also be converted into valuable bio-oil and bio-gas which can provide heat, electricity, and transportation fuel.

Herein, we propose a sustainable approach based on chrome-free LSW to design innovative electrodes in half-cell and full-cell LIBs. In particular, the main goal of this study is the investigation and comparison of the electrochemical properties of biochars obtained from leather waste through different approaches (*i.e.*, steam and CO_2 gas flow). Furthermore, in line with the philosophy of a reduced environmental impact, for preparing fully sustainable and environmentally friendly LIBs anodes, deionized water and carboxymethyl cellulose (CMC) have been used as alternatives to the toxic/teratogen *N*-methyl-2-pyrrolidone (NMP) and the biologically hazardous polyvinylidene fluoride (PVdF), respectively.[38] Indeed, the preparation of water-based electrodes does not require any controlled environment and, due to the higher vapour pressure of water in comparison with NMP, the water-based electrode drying process is much faster. This aspect determines an important consequence, namely a reduced energy consumption for the electrode preparation. Finally, for the full-cell preparation, we have coupled together the best performing steam-activated biochar anode with $LiFePO_4$ (LFP). All in all, we believe that this work supports the worldwide actions of reaching green LIBs at the cost of 100 $ kW per h by 2030.[39,40]

2. Experimental

2.1 Synthesis of biochar-based materials

The pyrolysis process was carried out by a laboratory-scale prototype plant (Carbolite custom model EVT 12/450B). The schematic of the laboratory-scale prototype is provided in Fig. S1 of the ESI.†

In a typical run, approximately 40 g of LSW was placed into the reactor. The feedstock used was supplied by PASUBIO S.p.A. tannery (Arzignano, Italy). Before pyrolysis, the LSW was sieved to <0.250 mm and then air-dried for 48 h. Afterward, the feedstock was pyrolyzed under a nitrogen flow of 100 mL min^{-1} at 700 °C at a heating rate of 5 °C min^{-1} and a residence time of 30 minutes. The obtained biochar was labelled as LSW-Biochar.

The LSW-Biochar was then physically activated by steam (LSW-ACS) or CO_2 (LSW-ACC) flow. For synthesizing LSW-ACS, LSW-Biochar was treated at 800 °C under a 57 vol% steam/N_2 mixture for four hours with a total gas flow of 160 mL min^{-1}. To prepare LSW-ACC, LSW-Biochar was activated under the same reaction conditions but using CO_2 gas as the activating agent. Thereafter, to remove the impurities from the surface of the biochars, sonication was performed with 1.0 M HCl solution for one hour. Finally, the samples were washed with deionized water and dried at 110 °C overnight.

2.2 Material characterization

The CHNS elemental analysis was carried out using a UNICUBE organic elemental analyzer (Elementar), with the oxygen content estimated by difference. The ash content was determined by using a thermo-gravimetric analyser (TGA 8000 PerkinElmer) according to the ASTM-D7582 protocol. The surface functionality was investigated by attenuated total reflection Fourier transform infrared spectroscopy (ATR-FTIR) using a PerkinElmer Frontier FTIR spectrometer over a wavenumber range of 400–4000 cm^{-1} at room temperature and a resolution of 4 cm^{-1}. X-ray photoelectron spectroscopy (XPS) was carried out using a Kratos Axis Ultra DLD spectrometer equipped with a monochromatic Al Kα source (15 kV, 20 mA) to investigate the presence of heteroatoms and their binding to the carbon matrix. Nitrogen physisorption measurements were performed at −196 °C by using a Micromeritics Tristar II Plus sorptometer (MICROMERITICS USA). The samples (~100 mg) were outgassed at 200 °C for 2 hours before the sorption experiment. The surface area was calculated by the BET and Langmuir equations and the total pore volume V_{tot} was measured according to the adsorbed amount of N_2 and P/P_0 (absolute pressure/saturation vapour pressure) values near 0.98.

An X-ray diffractometer (XRD, Malvern PANalytical Empyrean) equipped with a 1.8 kW CuKα sealed ceramic tube and a Renishaw *in via* micro Raman system equipped with a 532 nm laser source were used to determine the crystallinity, presence of minerals, and order/disorder degree of the structure of the samples.

The morphology of non-activated and activated carbons was investigated by a JEOL JSM-6490LA SEM analytical (low-vacuum) scanning electron microscope (SEM). The activated samples were also studied by field emission scanning electron microscopy (FE-SEM) using a JEOL JSM-7500 FA (Jeol, Tokyo, Japan), operating at 5–10 kV acceleration voltage and considering secondary electrons for enhancing the morphological structures.

2.3 Electrode preparation and cell assembly

The electrodes were prepared using an environmentally friendly method by mixing 70 wt% of biochar material, 20 wt% of conductive carbon black agent, and 10 wt% of CMC as the binder. After grinding the mixture with a mortar, deionized water was used as the solvent to form a slurry. Afterward, the mixture was stirred until reaching complete homogeneity and, through the doctor blade technique, a 200 μm layer was deposited on a copper foil, which was then dried for 3 h at 80 °C. Thereafter, the dried sheet was punched into circular discs with a diameter of 15 mm. The electrode discs were further dried under vacuum using a Buchi apparatus for 12 h at room temperature. At the end of this process, the discs were transferred in an argon-filled glove box (MBraun) with oxygen and water contents below 0.1 ppm. The mass loading of the active material was about 0.8–1 mg cm^{-2}. For the cell assembly, 2032 coin-cells were used for all the electrochemical tests with lithium metal chips as the anode, a microporous membrane (Celgard 3501) as a separator, and 1.0 M $LiPF_6$ solution in a 1 : 1 (v/v) ratio of ethylene carbonate : dimethyl carbonate (LP30) as the electrolyte (Merck, battery grade).

To investigate the performance of the biowaste in practical full-cell LIBs, we have selected the LSW-ACS anode electrode owing to its high electrochemical stability shown in the half-cell analysis. This electrode was pre-lithiated and then coupled with a commercial LFP (NEI corporation) used as the cathode. The mass loading of a single-coated LFP cathode on aluminium foil was 14.5 mg cm^{-2}. The pre-lithiation of the LSW-ACS anode was run with a very low discharge current density of 0.05 A g^{-1} (based on the LSW-ACS active mass) to ensure high reversibility of LSW-ACS *versus* lithium metal. After the discharge process, the Li/LSW-ACS cell was disassembled and the LSW-ACS electrode was rinsed with dimethyl carbonate in an argon-filled glove box. Afterward, the full-cell was assembled with LSW-ACS : LFP in a mass ratio of 1 : 3.6. This value was determined from the capacity ratio $Q_{anode} : Q_{cathode}$ at low current density. Finally, it should be highlighted that the active mass loading of the anode for the full cell was adjusted to 4 mg cm^{-2}. The same kinds of separator and electrolyte employed in the half-cell were used for the full-cell assembly.

2.4 Electrochemical measurements

Cyclic voltammetry (CV) measurements were conducted with 2032 coin-cells under the potential range of 0.01–3.00 V and a scan rate of 0.05 mV s^{-1}. The charge/discharge tests of the

half-cells were performed with a constant current (CC) protocol. The specific capacity of the half-cells was evaluated based on the mass of the biowaste active material. Furthermore, for the full-cell analysis, the CC protocol assumed a voltage range of 1.5–3.9 V at a current rate of 0.1 (equivalent to 0.1 C; 1C = 170 mA g_{LFP}^{-1}). Electrochemical impedance spectroscopy (EIS) was also used in the frequency range of 10 kHz to 100 mHz at an open circuit with a 10 mV alternating current (AC). The obtained impedance spectra were analysed using the Boukamp software, with a Chi-square goodness fit (χ^2) below 10^{-4}. All the electrochemical tests were performed by using a BCS-805 BioLogic instrument at room temperature and repeated three times to guarantee reproducibility.

3. Results and discussion

3.1 Material characterization

The CHNS elemental analysis of the synthesized products is shown in Table 1. As widely reported in the literature, the activation processes with steam and CO_2 involve oxidation reactions, resulting in porosity formation.[41] According to Table 1, the activation process with either steam or CO_2 determines the removal of nitrogen and sulphur from the pristine biochar, thus increasing the carbon content in the resulting samples. In particular, steam activation seems to remove more nitrogen and sulphur than the CO_2 process. This aspect can be ascribed to the smaller size of the water molecule in comparison with CO_2 which facilitates the activation through the diffusion of steam into the porous network.[24] Therefore, at this stage, LSW-ACC appears to be the material of choice, as both nitrogen and sulphur are beneficial for enhancing the lithium storage and improving the reversible capacity.[42] The situation seems however to change in favour of LSW-ACS when the elemental analysis is extended to O and C. Indeed, when CO_2 and steam are employed as oxidizing agents, they modify the oxygen-containing functional groups located on the activated surface. We found that LSW-ACC shows a higher O/C ratio compared to LSW-ACS, suggesting that more O-containing functional groups are present on the carbon surface by CO_2 activation. Importantly, high content of O can reduce the stability of the biochar, hence negatively affecting its electrochemical response.[43] The contribution of the activating agents to the carbonization degree was also analysed. A significant decrease in the H/C ratio after the activation process implies that the carbon structure becomes increasingly more aromatic and carbonaceous.[44] The lower H/C ratio of the LSW-ACS sample, compared to LSW-ACC, indicates a high degree of carbonization, suggesting a very condensate structure that can positively affect the electrochemical stability of LSW-ACS.

ATR-FTIR was then used to qualitatively analyse the functional groups on the carbon surface after the activation process. In the ATR-FTIR spectra of Fig. 1, the weak intense band around 3600 cm^{-1} is due to the vibrations of the O–H functional groups.[45] A strong band is observed at approximately 1600 cm^{-1}, which may be generated by the aromatic C=C stretching vibration and the C=O stretching of conjugated ketones and quinones.[46,47] Even though the activated samples show an IR profile similar to the pristine biochar, it is possible to observe some differences in the wavenumber range 2300 cm^{-1} to 800 cm^{-1}, typical of the surface functional groups of the structural network. The bands between 1700 cm^{-1} and 2300 cm^{-1} indicate the carboxyl and carbonyl groups. The broad band in the 1400–900 cm^{-1} region is due to a series of overlapping absorption bands that stemmed from the contemporary presence of C–O bonds that are typical of the alcohol, phenol, and ether bridges between the aromatic rings and the nitrogen group components (N–C and N-COO).[27,48]

Interestingly, these overlapping bands undergo a change in shape and intensity upon the occurrence of the activation process (blue and red lines), indicating a different distribution of nitrogen and oxygen functional groups on the material surface. Specifically, for LSW-ACC (red line), the maximum absorption shifts to a lower value (near 1140 cm^{-1}) than that of the pristine biochar (1210 cm^{-1}). The shift could be related

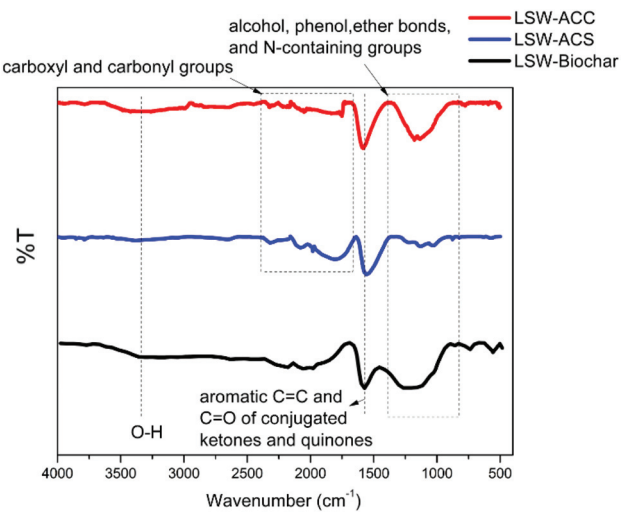

Fig. 1 ATR-FTIR spectra of LSW-ACC (red line), LSW-ACS (blue line), and LSW-Biochar (black line).

Table 1 CHNS elemental analysis of LSW-Biochar, LSW-ACS, and LSW-ACC

Sample	C [%]	N [%]	H [%]	S [%]	O [%]	Ash [%]	H/C	O/C
LSW-Biochar	71.6	11.0	1.8	1.1	5.8	8.7	0.025	0.08
LSW-ACS	77.8	4.0	1.3	0.6	4.7	11.6	0.016	0.06
LSW-ACC	73.4	7.4	1.3	1.0	5.3	11.6	0.018	0.07

to a minor contribution of N-bonds to the absorption band, in accordance with the lower content of nitrogen detected by CHNS elemental analysis. When LSW-ACS (blue line) is considered, the aforementioned overlapping bands consist of weak peaks at 1220, 1120, and 1020 cm^{-1}, suggesting a decrease in the number of surface functional groups with respect to LSW-ACC.

The effective heteroatom doping of LSW-biochar was investigated by XPS measurement. The X-ray photoemission high-resolution spectra of the oxygen, nitrogen, and sulphur energy regions are reported in Fig. S2,† together with the results of the best-fit procedure. Analysis of the N 1s region shows that N is effectively bound to carbon in several states (pyridinic N, amino N, pyrrolic N, and graphitic N). The low intensity peak at 402.6 ± 0.2 eV suggests that some nitrogen atoms are in the form of oxygenated compounds: pyridine *N*-oxide.[49] The sulphur signal is fitted with four different chemical states. The fitting revealed that the main sulphur peak is due to either C–S–C or thiophene (peaks at 163.70, and 164.5 eV). The presence of a peak at 532.6 eV in the O 1s spectrum could be attributed to the oxygen atoms of various oxygen groups, including C═O, O–C–O and O═C–O.[50] We should note that, in addition to S, N, and O groups, other elements such as Mo are also present in the carbonized biowaste.

Nitrogen physisorption analysis was carried out to determine the surface area and pore size distribution of the samples (Fig. 2). Importantly, the isotherm of the pristine LSW-Biochar (in the inset of Fig. 2) does not match with any profile in the IUPAC classification. The results indicate that LSW-Biochar is characterized by an extremely low surface area and total pore volume typical of non-porous materials. These kinds of results can also be found in different materials, such as in carbon samples obtained from the pyrolysis of leather processing waste.[51]

As depicted in Fig. 2, the N_2 adsorption–desorption isotherms of the activated carbons show a composite nature, exhibiting the combination of type I and type IV isotherms with an apparent hysteresis loop of type H4, suggesting the co-existence of a micro and mesoporous structure. The initial region of reversible micropore filling is followed by multilayer physisorption and capillary condensation. This is the typical profile for a micro/mesoporous activated carbon with a slit-like pore structure.[46]

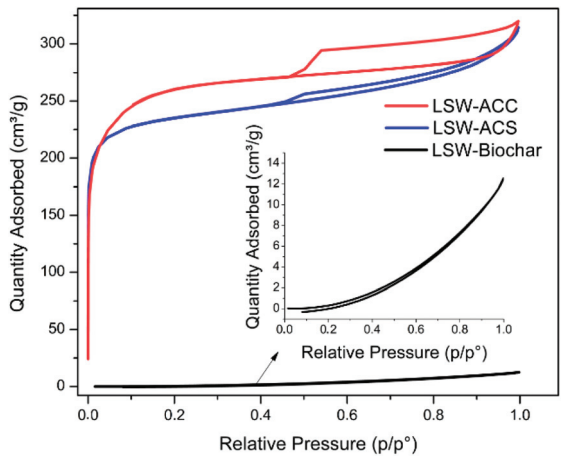

Fig. 2 Nitrogen adsorption–desorption isotherms of LSW-ACC (red line), LSW-ACS (blue line), and LSW-Biochar (black line).

As summarized in Table 2, both activated samples present high surface areas, large pore volumes, and wide average pore sizes. According to the BET surface analysis, the surface areas of LSW-ACS and LSW-ACC are equal to 726 and 858 $m^2\ g^{-1}$, respectively. The high surface area and the hierarchical distribution of the micro/mesoporous structures of both activated samples could provide plenty of sites for the charge-transfer reaction and shortening the diffusion length of lithium ions, respectively.

The XRD patterns (Fig. 3a) of the carbonized materials show the same features observed in most disordered carbon materials.[52] Two prominent broad diffraction peaks are present at 2θ ~25° and ~44°, which are related to the (002) and (100) reflection planes.[53] The shape of these peaks suggests the presence of a disordered turbostratic carbon structure.[54] According to Bragg's law,[55] the interlayer distance of graphitic layers (d_{002}) is calculated in the range ~0.351–0.359 nm. Moreover, the thickness (L_c), and the average width of the graphitic domains (L_a), calculated using the Scherrer equation,[56] are very similar for all samples, ~0.95–1.01 nm for L_c and 2.08–2.37 nm for L_a. The parameters calculated from each sample are reported in Table S1.† Based on these results, the carbonized samples are estimated to be composed of ~3 stacked graphene layers (*i.e.*, 0.98/0.36 = 2.72).[57] In addition to the (002) and (100) reflections, several sharp peaks are present in the XRD patterns, which can be ascribed to some inorganic phases such as NaCl (ICSD-41439), probably arising from HCl used in the synthesis process, and crystalline SiO_2 (quartz (ICSD 83849), and Trydimite (ICSD 176)), typical contaminations present in quartz reactors.

Raman spectroscopy (Fig. 3b) was then performed for the LSW-Biochar, LSW-ACS, and LSW-ACC electrodes with the objective to determine the carbon order and the amount of defects. The broad D band located around 1360 cm^{-1} is associated with the edges, defects, and disorders of carbonaceous materials.[58] On the contrary, the G band at about 1600 cm^{-1} corresponds to the graphitic layers and shows sp^2 hybridized carbon.[58,59] The intensity ratio of the D band and G band (I_D/I_G) is generally used to determine the level of disorder in the carbon (I_D/I_G is proportional to the disorder).[60] In this respect, the I_D/I_G ratio for LSW-ACC is equal to 0.91, a value higher than the corresponding ratio for LSW-ACS (I_D/I_G = 0.88). This

Table 2 Results of nitrogen physisorption analysis

Sample	S_{BET} ($m^2\ g^{-1}$)	$S_{Langmuir}$ ($m^2\ g^{-1}$)	S_{micro} ($m^2\ g^{-1}$)	V_{tot} ($cm^3\ g^{-1}$)	V_{micro} ($cm^3\ g^{-1}$)	V_{meso} ($cm^3\ g^{-1}$)
LSW-ACS	726	1.029	865	0.45	0.27	0.18
LSW-ACC	858	1.165	975	0.48	0.29	0.19

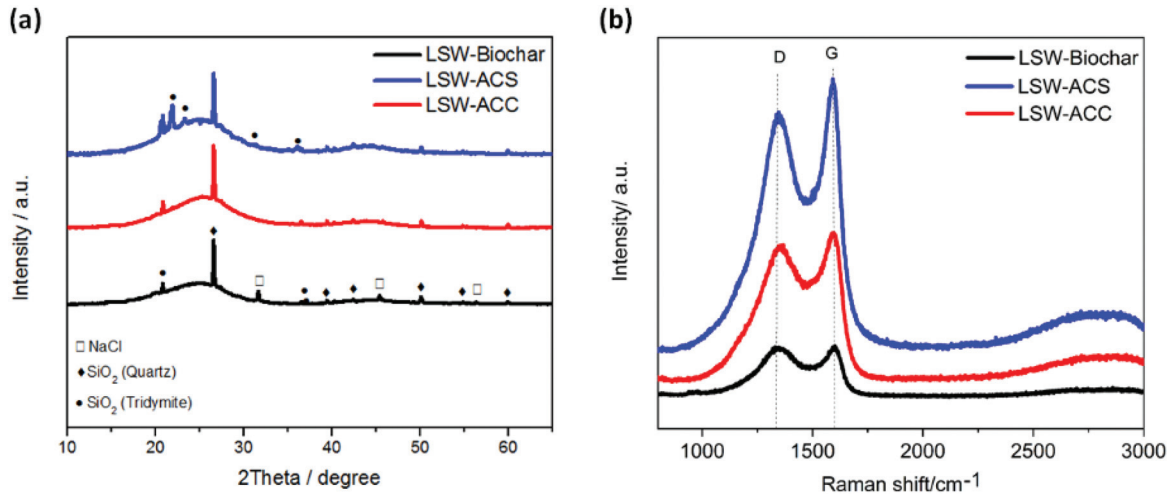

Fig. 3 (a) XRD patterns and (b) Raman patterns of LSW-ACS (blue line), LSW-ACC (red line), and LSW-Biochar (black line).

difference suggests a lower graphitic order for LSW-ACC, possibly due to the important contents of S and N elements in the graphene layers.[43] Another important quantity to consider is $I_D/(I_D + I_G)$ which describes the ratio of defects along the whole graphene sheets.[61] The $I_D/(I_D + I_G)$ values of LSW-Biochar, LSW-ACC and LSW-ACS are 0.50, 0.48 and 0.47, respectively.

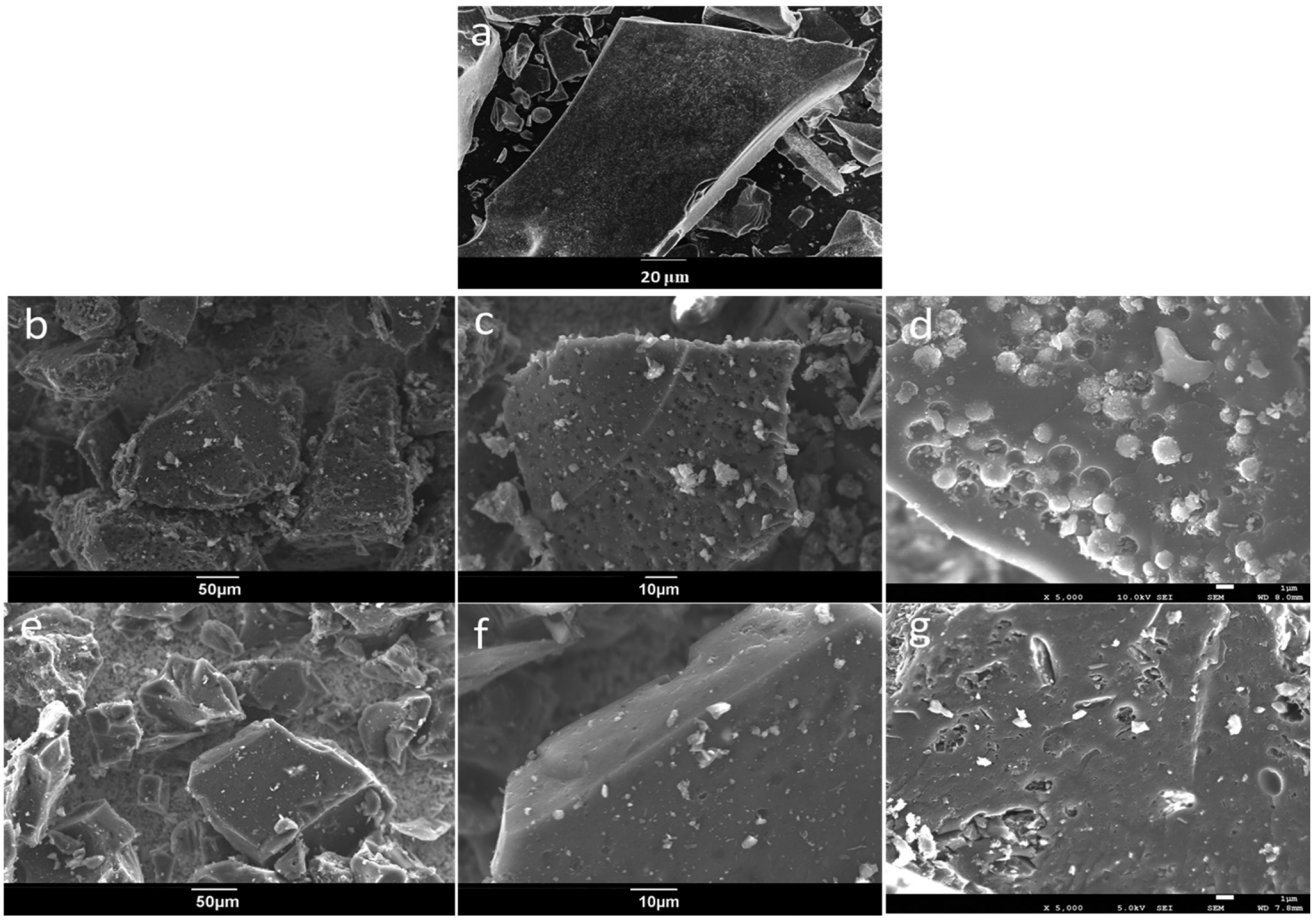

Fig. 4 SEM image of LSW-Biochar (a), SEM (b and c) and FESEM images (d) of the LSW-ACS sample. The SEM (e and f) and FESEM images (g) of the LSW-ACC sample.

These results show that the activation process and the elevated temperature can slightly diminish the number of defects. The higher defect density of LSW-ACC compared to LSW-ACS supports the idea that the degree of graphitization decreases with the increase in defect concentration. In this respect, and as previously reported,[62] N atoms cause a large number of defects in carbon structures, in turn increasing the number of active sites dedicated to Li storage. Even though, when it comes to the overall electrochemical evaluation of a material, a trade-off needs to be identified between having a high number of defects and a high degree of ordered graphitic carbon as both factors can contribute to the performance of the electrochemical cell.[42,62]

The morphological evolution of the activated carbon samples was observed by scanning electron microscope (SEM) and field emission scanning electron microscope (FESEM) images. According to the SEM images in Fig. 4, LSW-Biochar shows a morphology resembling broken glass shards without any distinguished pores on the surface. This result suggests that the pyrolysis step is not enough to create a well-defined porosity. On the other hand, in the activated samples, clear porosity can be observed. The SEM and FESEM images of LSW-ACS in Fig. 4(b–d) show a uniform distribution of olive-shaped pores on the biochar surface.[26] Furthermore, LSW-ACS seems to possess higher order porosity than LSW-ACC, thus confirming the results obtained by the Raman, N_2 adsorption–desorption isotherm, and elemental analysis techniques. The higher order porosity of LSW-ACS *vs.* LSW-ACC is associated with the smaller dimension of the H_2O molecule.[63,64] Indeed, its small dimension makes H_2O more effective than CO_2 in the removal of non-carbonaceous materials, therefore leading to the formation of higher order micro-porous structures on the biochar surface.[36] This is confirmed by Fig. 4(e–g), which shows the irregular surface of LSW-ACC owing to the different pore dimensions and channel sizes and relation to higher amounts of N, O, and S (see Table 1). Furthermore, it appears that the use of CO_2 as the activation agent, leads to the formation of more mesopores than micropores on the biochar surface. This would indeed confirm the previous Raman analysis where a higher amorphous grade was observed for LWS-ACC than for LWS-ACS.

3.2 Electrochemical performance

The electrochemical performance of LSW-Biochar, LSW-ACS, and LSW-ACC electrodes was evaluated by galvanostatic charge–discharge cycling, CV, and EIS techniques. Fig. 5a dis-

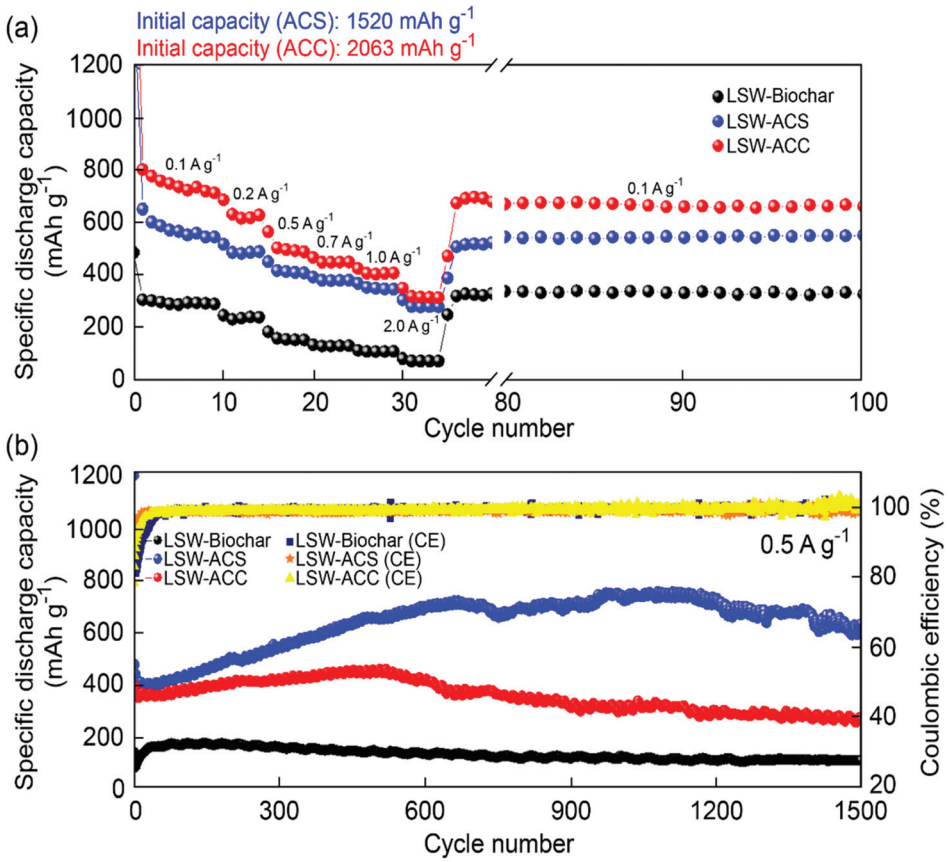

Fig. 5 (a) Rate capability of the carbonized samples over cycling at current densities of 0.1, 0.2, 0.5, 0.7, 1, and 2 A g^{-1} and (b) cycling performance (current density of 0.5 A g^{-1}) of the carbonized samples performed in lithium-metal half-cells at room temperature within 0.01–3 V. CE: coulombic efficiency.

plays the rate performance of LSW-Biochar, LSW-ACS, and LSW-ACC over cycling at different current densities. At 0.1, 0.2, 0.5, 0.7, 1, and 2 A g^{-1}, the specific discharge capacity of LSW-ACS is around 600, 490, 410, 380, 350, and 280 mA h g^{-1}, respectively, while for LSW-ACC the specific discharge capacity returns values around 760, 630, 500, 450, 407 and 319 mA h g^{-1}, respectively. In contrast, the non-activated electrode delivers much lower reversible capacities at all the investigated current densities. This confirms that CO_2 and steam activations lead to the enhancement of reversible Li-ion storage by altering the surface properties of the biochar such as surface texture, surface area and porosity. Finally, when the current density rolls back to 0.1 A g^{-1}, all three electrodes show excellent capacity retention of 100%.

The CV and the galvanostatic charge–discharge profiles of the three electrodes show the typical curve of carbon anode materials *versus* Li/Li^+.[65] Each profile is discussed in detail in the ESI, Fig. S3.†

The cycling performance of the biowaste electrodes at 0.5 A g^{-1} (equivalent to ~1.4 C *vs.* graphite) is reported in Fig. 5b. The cells with activated biochars demonstrate an initial discharge capacity of around 400 mA h g^{-1}, while the cell containing the LSW-Biochar electrode only shows a capacity of 100 mA h g^{-1} at 0.5 A g^{-1}. The lower capacity of the LSW-Biochar electrode is related to its low surface area and non-porous structure which provide less active sites for Li-ion storage compared to LSW-ACS and LSW-ACC. Interestingly, the activated carbon-based electrodes exhibit a capacity increase after the initial charge–discharge cycling process. This phenomenon has also been observed in previous studies where N and O rich porous carbon derived from biomasses was used as the electrode material in LIBs.[66–68] Possible reasons for this behaviour could be attributed to the easy access of the electrolyte to the unexposed micro and mesopores sites of the electrodes after several oxidation/reduction reactions.[69] Another reason can be the lowering of the internal resistance after cycling, as shown in the Nyquist plots of LSW-ACS and LSW-ACC (Fig. S4 and Table S2†). Finally, after 1500 charge and discharge cycles, LSW-Biochar, LSW-ACS, and LSW-ACC could provide capacities equal to 108, 625, and 267 mA h g^{-1}, respectively.

It can be noticed that a direct comparison between Fig. 5a and b reveals what might appear as a controversial behaviour when observing the ratio between the specific capacities of LSW-ACC and LSW-ACS. Indeed, while in Fig. 5a the electrochemical response of LSW-ACC is better than that of LSW-ACS, the opposite appears to occur in Fig. 5b. The explanation lies in the low-rate activation shown in Fig. 5a, where the initial test was performed at 0.1 A g^{-1}, whereas in Fig. 5b the test was immediately set at 0.5 A g^{-1}. In order to confirm this thesis, we analysed the same kind of samples by starting at the initial rate of 0.1 A g^{-1}, as shown in the ESI (Fig. S5†).

Table 3 lists the most recent reports on exploiting waste materials for anode preparation in lithium half-cell batteries. In this respect, the steady increase of published literature in this field demonstrates the enormous potential associated with the green re-use of wasting materials in LIBs. In particu-

Table 3 Comparison of the preparation methods and the main electrochemical criteria of different waste-based anode electrodes in lithium half-cell batteries

Sample	Preparation method	Initial discharge capacity (mA h g^{-1}) at low current density	Current density (A g^{-1}) & corresponding reversible capacity (mA h g^{-1}/cycles)	Ref.
Tannery	Pyrolysis at 700 °C and CO_2 activation	2063 at 0.1 A g^{-1}	0.5 & 452/450th	This work
	Pyrolysis at 700 °C and steam activation	1520 at 0.1 A g^{-1}	0.5 & 625/1500th	
Rice husk	Multi-step heat treatment and carbonization under Ar gas at 600 °C	1627 at 0.075 A g^{-1}	0.075 & 757/150th	71
Wheat straw	KOH activation and carbonization at 800 °C in the inert N_2 atmosphere	797 at 0.037 A g^{-1} (0.1 C)	0.037 (0.1 C) & 310/100th	72
Leather	Carbonation at 1000 °C under Ar atmosphere	~750 at 0.05 A g^{-1}	0.05 & 327/50th	35
Garlic peel	KOH activation and carbonization at 850 °C in the Ar atmosphere	1825 at 0.05 A g^{-1}	0.1 & 540/100th	73
Corn stalk core	Calcination at 550 °C under N_2 atmosphere and KOH activation	1614.1 at 0.075 A g^{-1}	0.075 & 504/100th	74
Bamboo shoot hulls	Heat treatment and carbonization at 600 °C under Ar atmosphere	1319 at 0.2 A g^{-1}	3 & ~250/1000th	75
Hazelnut shell	Annealing under Ar/H_2, carbonization at 900 °C, laser irradiation	1108 at 0.01 A g^{-1}	0.01 & 578/20th	76
Rice husk	Carbonization at 600 °C under N_2 atmosphere and hydrothermal NaOH treatment	1647 at 0.075 A g^{-1} (0.2C)	0.075 & 502/100th	77
Tannin-furanic resins	Heat treatment and carbonization at 1000 °C under Ar atmosphere	605 at 0.05 A g^{-1}	0.4 & 134/200th	78
Spruce hard carbon	H_3PO_4 activation and pyrolysis at 1100 °C	~385 at 0.037 A g^{-1} (0.1 C)	0.037 A g^{-1} (0.1 C) & ~300/400th	79
Tea-seed shells	Calcination at 800 °C under flow and KOH activation	913 at 0.037 A g^{-1} (0.1 C)	0.037 (0.1 C) & 537/100th	80
Coffee ground	Carbonization at 800 °C under N_2 atmosphere	764 at 0.1 A g^{-1}	0.1 & 262/100th	81

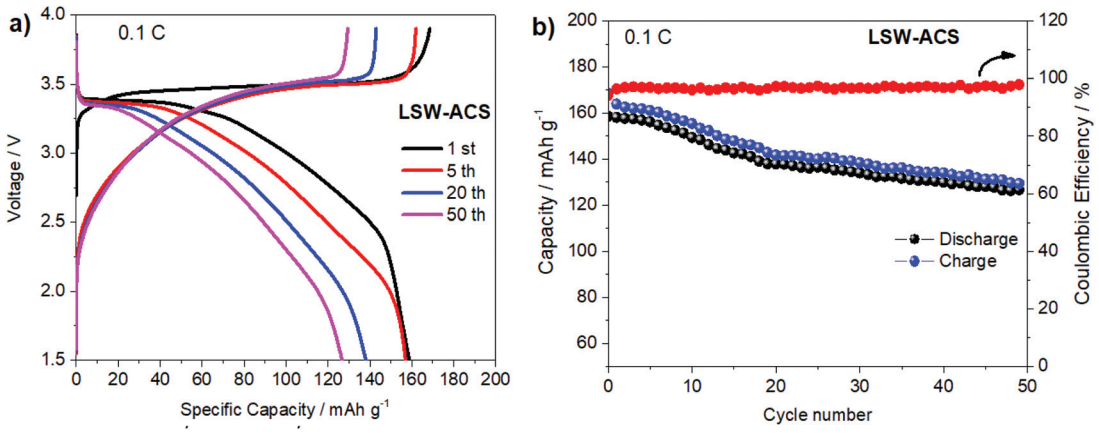

Fig. 6 (a) Galvanostatic charge–discharge profile and (b) cycling performance of LSW-ACS/LFP full-cell in the range of 1.5–3.9 V at 0.1 C (1C = 170 mA g_{LFP}^{-1}) and room temperature. LFP = 14.5 mg cm^{-2} and LSW-ACS = 4 mg cm^{-2}. The specific capacity of the cell is reported according to LFP active mass.

lar, the reported performance shows that the sustainable approach for material and electrode preparation illustrated in this work represents a sensible improvement with respect to most papers reported to date. Importantly, it must also be noted that the environmentally friendly route for material preparation is often ignored in previous studies.

The remarkable results achieved herein could be related to the optimum content of heteroatoms (N, O, and S), the effective porous architecture, and the strong structural integrity of the engineered materials. Indeed, these features improve the electrochemical performance of the electrode by providing the adequate number of active sites. In order to provide a scenario as complete as possible, the results achieved with lithium-metal half-cells were then verified in a full-cell configuration. Specifically, the full-cell employed high mass LFP loading as the cathode, LSW-ACS as the anode, and LP30 as the electrolyte. In particular, LSW-ACS was chosen over LSW-ACC for its long cycling better performance. Fig. 6a depicts the galvanostatic charge–discharge curves of the LSW-ACS/LFP full-cell during the 1^{st}, 5^{th}, 20^{th}, and 50^{th} cycles in the voltage range of 1.5–3.9 V at 0.1 C. In the first cycle, the charge and discharge capacities are 169, and 159 mA h g^{-1}, respectively, providing a coulombic efficiency as high as 94%. The average working potential of the cell is approximately 3.4 V. Interestingly, the results are similar to previously reported data where a low mass LFP loading was combined with a graphite anode in a full-cell system.[70] As shown in Fig. 6b, after 50 cycles of charge/discharge, the biowaste-based full-cell maintains 80% of its initial capacity with a coulombic efficiency above 98%. Table S3† compares the initial capacity and durability of the LSW-ACS/LFP full-cell with the state-of-the-art full-cell LIBs employing graphite. The table suggests that the biochar derived from leather waste through the engineering approach reported herein could be considered one of the promising candidates to be used as the anode material for lithium metal-free bio-based batteries.

4. Conclusions

In this work, the physical and electrochemical properties of carbon material (biochar) derived from chrome-free leather shaving waste were investigated for applications in LIBs. The main motivation was the desire to address environmental sustainability and circular economy. In this respect, a fully sustainable and green approach was developed to design bio-based electrodes to be tested in both half and full-cell configurations. In particular, two environmentally friendly activation methods were employed, based either on H_2O or CO_2. For both cases, the assembled lithium-metal half-cells have demonstrated good rate capability and cycling performance, with the H_2O-based cell providing the best long cycling result. Furthermore, as a practical example, a full-cell based on a high mass LFP loading cathode and a H_2O-activated anode was realized. The results showed an initial discharge capacity of about 160 mA h g^{-1} with an acceptable cycling stability at 0.1 C. The promising performance reported in this work is associated with the synergistic effect of defects, interlayer spacing, heteroatoms-doped (N, O, and S), high specific surface area, and hierarchical micro/mesopore structure of the activated biochars. We believe that this work represents an important step forward, indeed a step closer to practical LIBs with negligible environmental impact. Finally, it is worth noting that these findings could also be extensively applied to different kinds of electrochemical energy storage devices, such as Na-ion batteries, lithium-metal free sulphur batteries, or fuel cells, hence not limited to conventional LIBs only.

Author contributions

P. S., S. T., and S. T.: conceptualization, methodology, writing original draft, review & editing, data curation, investigation, and visualization. E. V., and S. F.: review & editing. S. L.: SEM

analysis. M. P., and S. M.: X-ray characterization; T. L.: review & editing. M. S.: resources and review; P. C.: review, and R. P. Z.: supervision, validation, resources, and review & editing.

Conflicts of interest

Three are no conflicts to declare.

Acknowledgements

This research was supported by the European LIFE program entitled LIFE GOAST – Green Organic Agents for Sustainable Tanneries (LIFE ENV/IT/000416). The authors wish to thank Dr Elena Ghedini and all partners involved in the LIFEGOAST project for their excellent scientific and technical assistance. The authors gratefully acknowledge PASUBIO S.p.A for supplying leather shaving waste. R. P. Z. would like to acknowledge the support from the NSFC project, grant no. 32071317.

References

1 J. Jurasz, F. A. Canales, A. Kies, M. Guezgouz and A. Beluco, *Sol. Energy*, 2020, **195**, 703–724.
2 F. Lorandi, T. Liu, M. Fantin, J. Manser, A. Al-Obeidi, M. Zimmerman, K. Matyjaszewski and J. F. Whitacre, *iScience*, 2021, **24**, 102578.
3 Y. Xi, S. Huang, D. Yang, X. Qiu, H. Su, C. Yi and Q. Li, *Green Chem.*, 2020, **22**, 4321–4330.
4 S. Li, F. Lorandi, H. Wang, T. Liu, J. F. Whitacre and K. Matyjaszewski, *Prog. Polym. Sci.*, 2021, **122**, 101453.
5 S. Javadian, P. Salimi, H. Gharibi, A. Fathollahi, E. Kowsari and J. Kakemam, *J. Iran. Chem. Soc.*, 2019, **16**, 2123–2134.
6 S. Javadian, Z. Parviz, P. Salimi, M. Nasrollahpour, H. Gharibi, H. Kashani, A. Morsali and R. P. Zaccaria, *J. Alloys Compd.*, 2022, **898**, 162849.
7 V. Mullaivananathan, R. Sathish and N. Kalaiselvi, *Electrochim. Acta*, 2017, **225**, 143–150.
8 P. Salimi and E. Kowsari, *J. Electron. Mater.*, 2019, **48**, 2254–2262.
9 M. K. Rybarczyk, H. J. Peng, C. Tang, M. Lieder, Q. Zhang and M. M. Titirici, *Green Chem.*, 2016, **18**, 5169–5179.
10 X. Zhou, F. Chen, T. Bai, B. Long, Q. Liao, Y. Ren and J. Yang, *Green Chem.*, 2016, **18**, 2078–2088.
11 O. Norouzi, P. Salimi, F. Di Maria, S. E. M. Pourhosseini and F. Safari, *Production of Materials from Sustainable Biomass Resources*, ed. Z. Fang, R. L. Smith Jr. and X.-F. Tian, Springer, 2019, pp. 233–265, ISBN: 978-981-13-3768-0.
12 J. Niu, R. Shao, J. Liang, M. Dou, Z. Li, Y. Huang and F. Wang, *Nano Energy*, 2017, **36**, 322–330.
13 J. H. Um, C. Y. Ahn, J. Kim, M. Jeong, Y. E. Sung, Y. H. Cho, S. S. Kim and W. S. Yoon, *RSC Adv.*, 2018, **8**, 32231–32240.
14 H. Chen, R. Liu, Y. Wu, J. Cao, J. Chen, Y. Hou, Y. Guo, R. Khatoon, L. Chen, Q. Zhang, Q. He and J. Lu, *Chem. Eng. J.*, 2021, **407**, 126973.
15 P. Salimi, O. Norouzi and S. E. M. Pourhosseini, *J. Alloys Compd.*, 2019, **786**, 930–937.
16 Y. Zhang, M. Xie, Y. He, Y. Zhang, L. Liu, T. Hao, Y. Ma, Y. Shi, Z. Sun, N. Liu and Z. John Zhang, *Chem. Eng. J.*, 2021, **420**, 130469.
17 U. Kumar, D. Goonetilleke, V. Gaikwad, J. C. Pramudita, R. K. Joshi, N. Sharma and V. Sahajwalla, *ACS Sustainable Chem. Eng.*, 2019, **7**, 10310–10322.
18 Y. Yao and F. Wu, *Nano Energy*, 2015, **17**, 91–103.
19 S. J. Yang, M. Antonietti and N. Fechler, *J. Am. Chem. Soc.*, 2015, **137**, 8269–8273.
20 B. Zhu, K. Li, J. Liu, H. Liu, C. Sun, C. E. Snape and Z. Guo, *J. Mater. Chem. A*, 2014, **2**, 5481–5489.
21 J. Liu, N. P. Wickramaratne, S. Z. Qiao and M. Jaroniec, *Nat. Mater.*, 2015, **14**, 763–774.
22 Z. Y. Sui, Q. H. Meng, J. T. Li, J. H. Zhu, Y. Cui and B. H. Han, *J. Mater. Chem. A*, 2014, **2**, 9891–9898.
23 A. Gomez-Martin, J. Martinez-Fernandez, M. Ruttert, M. Winter, T. Placke and J. Ramirez-Rico, *Chem. Mater.*, 2019, **31**, 7288–7299.
24 B. Sajjadi, W. Y. Chen and N. O. Egiebor, *Rev. Chem. Eng.*, 2019, **35**, 735–776.
25 J. Deng, M. Li and Y. Wang, *Green Chem.*, 2016, **18**, 4824–4854.
26 S. E. M. Pourhosseini, O. Norouzi, P. Salimi and H. R. Naderi, *ACS Sustainable Chem. Eng.*, 2018, **6**, 4746–4758.
27 P. Salimi, S. Javadian, O. Norouzi and H. Gharibi, *Environ. Sci. Pollut. Res.*, 2017, **24**, 27974–27984.
28 S. E. M. Pourhosseini, O. Norouzi and H. R. Naderi, *Biomass Bioenergy*, 2017, **107**, 287–298.
29 A. L. Tasca and M. Puccini, *J. Cleaner Prod.*, 2019, **226**, 720–729.
30 G. Liknaw, T. Tekalign and K. Guya, *J. Environ. Earth Sci.*, 2017, **7**, 88–97.
31 M. A. Moktadir, H. B. Ahmadi, R. Sultana, F. T. Zohra, J. J. H. Liou and J. Rezaei, *J. Cleaner Prod.*, 2020, **251**, 119737.
32 K. J. Sreeram and T. Ramasami, *Resour., Conserv. Recycl.*, 2003, **38**, 185–212.
33 Y. Yang, H. Ma, X. Chen, C. Zhu and X. Li, *Environ. Res.*, 2020, **183**, 109159.
34 L. Rosu, C. Varganici, A. Crudu, D. Rosu and A. Bele, *J. Cleaner Prod.*, 2018, **177**, 708–720.
35 M. Ashokkumar, N. T. Narayanan, A. L. Mohana Reddy, B. K. Gupta, B. Chandrasekaran, S. Talapatra, P. M. Ajayan and P. Thanikaivelan, *Green Chem.*, 2012, **14**, 1689–1695.
36 N. Konikkara, L. J. Kennedy and J. J. Vijaya, *J. Hazard. Mater.*, 2016, **318**, 173–185.
37 R. Soni, S. N. Bhange and S. Kurungot, *Nanoscale*, 2019, **11**, 7893–7902.
38 D. Bresser, D. Buchholz, A. Moretti, A. Varzi and S. Passerini, *Energy Environ. Sci.*, 2018, **11**, 3096–3127.

39 G. Berckmans, M. Messagie, J. Smekens, N. Omar, L. Vanhaverbeke and J. Van Mierlo, *Energies*, 2017, **10**, 1314.
40 D. L. Wood, J. Li and C. Daniel, *J. Power Sources*, 2015, **275**, 234–242.
41 N. L. Panwar and A. Pawar, *Biomass Convers. Biorefin.*, 2022, **12**, 925–947.
42 H. Wan and X. Hu, *Solid State Ionics*, 2019, **341**, 115030.
43 H. Shan, X. Li, Y. Cui, D. Xiong, B. Yan, D. Li, A. Lushington and X. Sun, *Electrochim. Acta*, 2016, **205**, 188–197.
44 D. Angin, *Bioresour. Technol.*, 2013, **128**, 593–597.
45 J. M. de la Rosa, M. Paneque, A. Z. Miller and H. Knicker, *Sci. Total Environ.*, 2014, **499**, 175–184.
46 Y. Liu, Z. He and M. Uchimiya, *Mod. Appl. Sci.*, 2015, **9**, 246–253.
47 B. Ma, Y. Huang, Z. Nie, X. Qiu, D. Su, G. Wang, J. Yuan, X. Xie and Z. Wu, *RSC Adv.*, 2019, **9**, 20424–20431.
48 T. L. P. Dantas, F. M. T. Luna, I. J. Silva, D. C. S. de Azevedo, C. A. Grande, A. E. Rodrigues and R. F. P. M. Moreira, *Chem. Eng. J.*, 2011, **169**, 11–19.
49 P. Wang, J. Bai, K. Li, H. Ma, W. Li, X. Zhu, Y. Sun and B. Zhao, *Chem. Eng. J.*, 2021, **425**, 130607.
50 S. W. Lee, N. Yabuuchi, B. M. Gallant, S. Chen, B. S. Kim, P. T. Hammond and Y. Shao-Horn, *Nat. Nanotechnol.*, 2010, **5**, 531–537.
51 L. J. Kennedy, T. Ratnaji, N. Konikkara and J. J. Vijaya, *J. Cleaner Prod.*, 2018, **197**, 930–936.
52 P. González-García, S. Gamboa-González, I. Andrade Martínez and T. Hernández-Quiroz, *Environ. Prog. Sustainable Energy*, 2020, **39**, 1–13.
53 L. Huang, Y. Sun, W. Wang, Q. Yue and T. Yang, *Chem. Eng. J.*, 2011, **171**, 1446–1453.
54 E. Hao, W. Liu, S. Liu, Y. Zhang, H. Wang, S. Chen, F. Cheng, S. Zhao and H. Yang, *J. Mater. Chem. A*, 2017, **5**, 2204–2214.
55 C. Marino, J. Cabanero, M. Povia and C. Villevieille, *J. Electrochem. Soc.*, 2018, **165**, A1400–A1408.
56 C. Liu, G. Han, Y. Chang, Y. Xiao, M. Li, W. Zhou, D. Fu and W. Hou, *ChemElectroChem*, 2016, **3**, 323–331.
57 E. M. Lotfabad, J. Ding, K. Cui, A. Kohandehghan, W. P. Kalisvaart, M. Hazelton and D. Mitlin, *ACS Nano*, 2014, **8**, 7115–7129.
58 A. K. Mondal, K. Kretschmer, Y. Zhao, H. Liu, H. Fan and G. Wang, *Microporous Mesoporous Mater.*, 2017, **246**, 72–80.
59 X. Gu, C. J. Tong, S. Rehman, L. M. Liu, Y. Hou and S. Zhang, *ACS Appl. Mater. Interfaces*, 2016, **8**, 15991–16001.
60 Y. Gong, D. Li, C. Luo, Q. Fu and C. Pan, *Green Chem.*, 2017, **19**, 4132–4140.
61 S. Qiu, L. Xiao, M. L. Sushko, K. S. Han, Y. Shao, M. Yan, X. Liang, L. Mai, J. Feng, Y. Cao, X. Ai, H. Yang and J. Liu, *Adv. Energy Mater.*, 2017, **7**, 1–11.
62 J. Zhao, Y. Liu, X. Quan, S. Chen, H. Zhao and H. Yu, *Electrochim. Acta*, 2016, **204**, 169–175.
63 D. Gąsior and W. J. Tic, *Econ. Environ. Stud.*, 2017, **17**, 597–611.
64 F. L. Braghiroli, H. Bouafif, C. M. Neculita and A. Koubaa, *Water, Air, Soil Pollut.*, 2019, **230**, 1–14.
65 W. Yu, H. Wang, S. Liu, N. Mao, X. Liu, J. Shi, W. Liu, S. Chen and X. Wang, *J. Mater. Chem. A*, 2016, **4**, 5973–5983.
66 C. Choi, S. D. Seo, B. K. Kim and D. W. Kim, *Sci. Rep.*, 2016, **6**, 1–10.
67 X. Sun, X. Wang, N. Feng, L. Qiao, X. Li and D. He, *J. Anal. Appl. Pyrolysis*, 2013, **100**, 181–185.
68 J. Ou, Y. Zhang, L. Chen, Q. Zhao, Y. Meng, Y. Guo and D. Xiao, *J. Mater. Chem. A*, 2015, **3**, 6534–6541.
69 B. Campbell, R. Ionescu, Z. Favors, C. S. Ozkan and M. Ozkan, *Sci. Rep.*, 2015, **5**, 1–9.
70 T. Wang, X. Yu, M. Fan, Q. Meng, Y. Xiao, Y. X. Yin, H. Li and Y. G. Guo, *Chem. Commun.*, 2019, **56**, 245–248.
71 K. Yu, Y. Wang, X. Wang, W. Liu, J. Liang and C. Liang, *Mater. Lett.*, 2019, **253**, 405–408.
72 P. Yan, F. Ai, C. Cao and Z. Luo, *J. Mater. Sci.: Mater. Electron.*, 2019, **30**, 14120–14129.
73 V. Selvamani, R. Ravikumar, V. Suryanarayanan, D. Velayutham and S. Gopukumar, *Electrochim. Acta*, 2016, **190**, 337–345.
74 Y. Li, C. Li, H. Qi, K. Yu and C. Liang, *Chem. Phys.*, 2018, **506**, 10–16.
75 W. Chen, D. Xu, S. Kuang, Z. Wu, H. Hu, M. Zheng and X. Yu, *J. Power Sources*, 2021, **489**, 229459.
76 M. Curcio, S. Brutti, L. Caripoti, A. De Bonis and R. Teghil, *Nanomaterials*, 2021, **11**, 3183.
77 Y. Li, F. Wang, J. Liang, X. Hu and K. Yu, *New J. Chem.*, 2016, **40**, 325–329.
78 Q. Huang, J. Hu, S. Wen, X. Zhang, G. Liu, S. Chang and Y. Liu, *Front. Chem.*, 2020, **8**, 1–10.
79 M. Drews, J. Büttner, M. Bauer, J. Ahmed, R. Sahu, C. Scheu, S. Vierrath, A. Fischer and D. Biro, *ChemElectroChem*, 2021, **8**, 4750–4761.
80 X. Lu, K. Xiang, W. Zhou, Y. Zhu and X. Chen, *Mater. Technol.*, 2018, **7857**, 1–8.
81 F. Luna-Lama, D. Rodríguez-Padrón, A. R. Puente-Santiago, M. J. Muñoz-Batista, A. Caballero, A. M. Balu, A. A. Romero and R. Luque, *J. Cleaner Prod.*, 2019, **207**, 411–417.